

A Smart Paclitaxel-Disulfiram Nanococrystals for Efficient MDR Reversal and Enhanced Apoptosis

Imran Shair Mohammad¹ · Wei He¹ · Lifang Yin^{1,2}

Received: 14 December 2017 / Accepted: 12 February 2018 / Published online: 27 February 2018
© Springer Science+Business Media, LLC, part of Springer Nature 2018

ABSTRACT

Purpose A multidrug resistance (MDR) modulator, disulfiram (DSF), was incorporated into pure paclitaxel (PTX) nanoparticles to construct a smart paclitaxel-disulfiram nanococrystals (PTX-DSF Ns) stabilized by β -lactoglobulin (β -LG), with the aim to reverse MDR and therefore enhance cytotoxicity towards Taxol-resistant A549 cells (A549/TAX).

Method PTX-DSF Ns was prepared by antisolvent precipitation method. Flow cytometry was used to determine the cell uptake, drug efflux inhibition, cell cycle phase arrest and apoptosis. MDR-1 gene expression level was detected by real time quantitative PCR and gel electrophoresis.

Results PTX-DSF Ns prepared from the optimized formulation had an optimum diameter of 160 nm, was stable and had a high drug-loading capacity. Importantly, the uptake of PTX-DSF Ns in A549/TAX cells was 14-fold greater than the uptake of PTX Ns. Furthermore, PTX-DSF Ns promoted 5-folds increase in apoptosis, enabled 7-folds reduction in the IC₅₀, and rendered 8.9-fold decrease in the dose compared with free PTX.

Conclusion PTX-DSF Ns with a precise mass ratio offer efficient cytotoxicity against Taxol-resistant cells and a novel approach for codelivery and sensitizing MDR

cancer to chemotherapy. In addition, the use of nanosuspensions as a combined treatment provides a new research avenue for nanosuspensions.

KEYWORDS apoptosis · combined therapy · multidrug resistance · nanosuspensions · p-glycoprotein

ABBREVIATIONS

A549	Sensitive human lung adenocarcinoma cell line
A549/TAX	Taxol resistant human lung adenocarcinoma cell line
ABC	ATP-Binding Cassette
BCA	Bicinchoninic acid
β -LG	β -lactoglobulin
CD	Circular Dichroism
cDNA	Complementary DNA
CI	Combination index
CLSM	Confocal laser scanning microscope
DAPI	4, 6-diamidino-2-phenylindole
DL	Drug loading
DLS	Dynamic light scattering
DMSO	Dimethyl sulfoxide
DRI	Dose reduction index
DSF	Disulfiram
EE	Encapsulation efficiency
FBS	Fetal bovine serum
FDA	Food and Drug administration
FITC	Fluorescein 5(6)-isothiocyanate
HPLC	High-performance liquid chromatography
IC ₅₀	Half maximal inhibitory concentration
MDR	Multidrug resistance
MDR-1	Multidrug resistance gene-1
MTT	3-(4, 5-dimethylthiazol-2-yl)-2, 5-diphenyltetrazolium bromide
PBS	Phosphate buffer saline
PDI	Polydispersity index

Electronic supplementary material The online version of this article (<https://doi.org/10.1007/s11095-018-2370-0>) contains supplementary material, which is available to authorized users.

✉ Wei He
weihe@cpu.edu.cn

✉ Lifang Yin
lifangyin_@163.com

¹ Department of Pharmaceutics, School of Pharmacy, China Pharmaceutical University, Nanjing 210009, People's Republic of China

² Key Laboratory of Druggability of Biopharmaceutics, China Pharmaceutical University, Nanjing 210009, People's Republic of China

P-gp	P-glycoprotein
PI	Propidium iodide
PTX	Paclitaxel
PTX-DSF	Free Paclitaxel-Disulfiram formulation
PTX-DSF	Paclitaxel-Disulfiram nanocrystals
Ns	
PXRD	Powder X-ray Diffraction
RNA	Ribonucleic acid
RT-qPCR	Real time quantitative PCR
SEM	Scanning electron microscopy
TEM	Transmission electron microscopy
Trp	Tryptophan

INTRODUCTION

Lung cancer is the leading cause of cancer-related deaths in the world (1). Chemotherapy is an effective measure to prolong survival in patients with lung cancer (2). However, the success of chemotherapy is hindered by the development of MDR during treatment (3). It is estimated that MDR is responsible for over 90% of treatment failure in patients with metastatic cancers, especially lung cancer (4). Accordingly, the reversal of MDR is a key determinant that sensitizes MDR tumor cells to chemotherapeutics. P-glycoprotein (P-gp)-mediated drug efflux, an overexpression of transporter protein encoded by MDR-1 gene, allows the efflux of chemotherapeutics from tumor cells and is a crucial factor that is responsible for MDR (5). Therefore, downregulating the P-gp is a promising strategy for MDR reversal.

DSF is a poorly water-soluble drug with a water-solubility of 0.2 mg/mL, which was approved by the FDA as a treatment for alcoholism in 1951 and has the potential to reverse MDR (6). DSF is capable of suppressing P-gp-mediated drug efflux by interacting with the cysteine moiety within P-gp and restoring the sensitivity of cancer cells to chemotherapeutics (7,8).

Consequently, we hypothesized that a combination of conventional chemotherapeutics, such as PTX with DSF, would be a smart approach to reverse MDR and enhance apoptosis. However, the cocktail approach is limited by various drawbacks, including different physicochemical properties of paired drugs, different pharmacokinetics and biodistribution of drug combinations, and different membrane transport mechanisms, leading to suboptimal co-drug concentrations at the target site (9,10). Nanocarriers are a potent tool for codelivery of multiple drugs, due to their outstanding merits, including the nanoscale size of the particles that allows specific accumulation at the target site, decreased side effects, alterations in performance *in vivo*, and enhanced solubility and drug stability (11–13). However, these conventional nanoparticles have limited drug-loading ability of less than 10% and potentially induce toxicity in normal tissues (14). Furthermore,

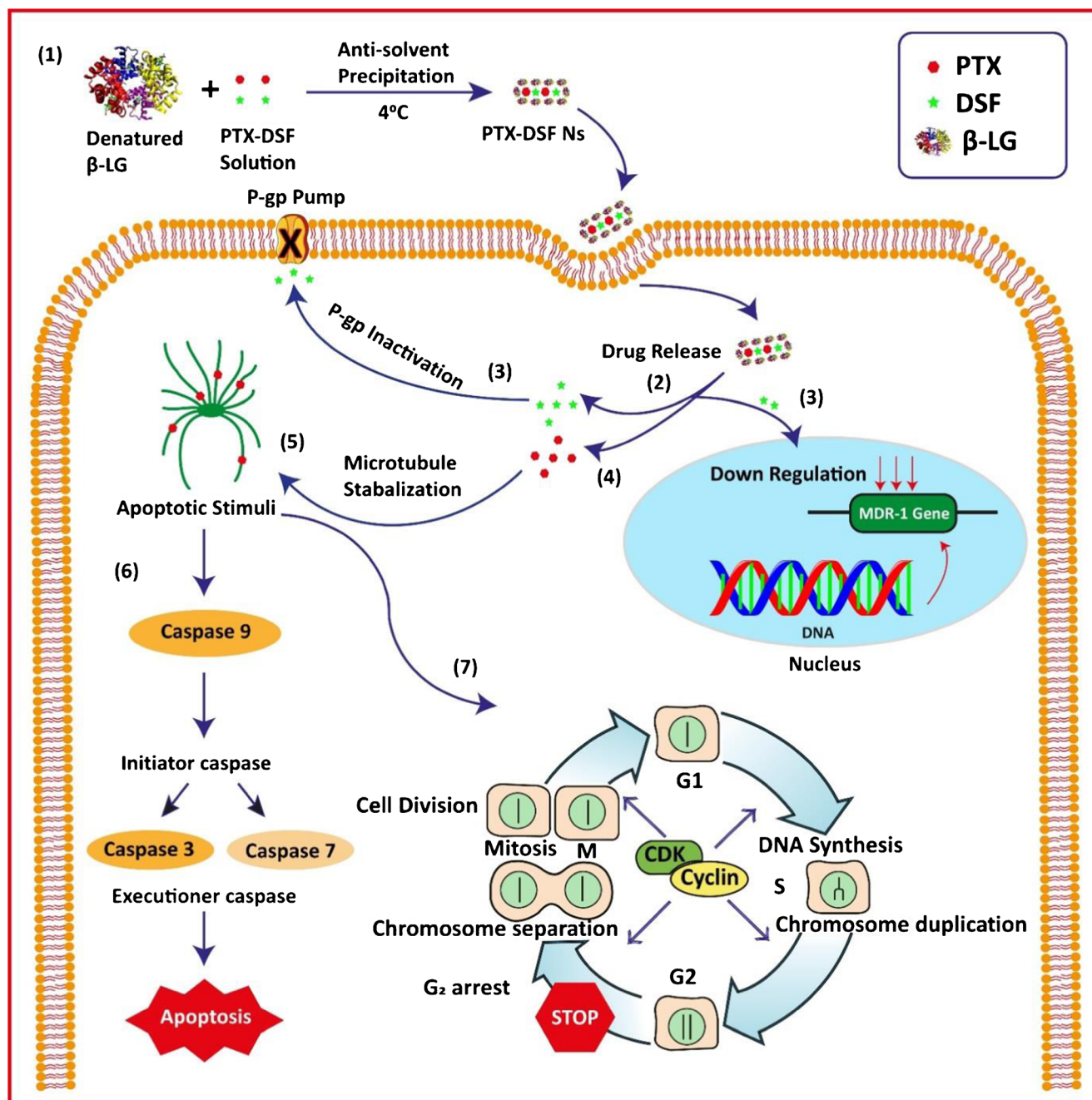
the synergistic effect between two drugs is strongly dependent on the dose ratio (15). Therefore, an accurate ratio of two combined drugs is critical for developing a perfect combinatory drug delivery system.

Nanosuspensions of insoluble active compounds are a colloidal dispersion consisting of nanocrystals and a minimal amount of stabilizers (16). In contrast with other nanomedicines, such as liposomes, polymer micelles, and inorganic nanocarriers, nanosuspensions have a markedly higher drug-loading capacity because they mainly consist of pure drug particles (17,18). Other advantages of nanosuspensions include reduced personal variability and food effects, improved treatment outcomes with decreased side effects, and low toxicity to normal organs; thus, nanosuspensions represent promising nanomedicines (19–23). As shown in our previous reports, β -LG coats drug particles in nanosuspensions and significantly prolongs the half-life in the blood circulation (24). Here, we designed PTX-DSF Ns employing β -LG as a stabilizer, which possessed a high drug-loading capacity at a precise co-drug ratio for MDR reversal and enhanced cytotoxicity toward Taxol-resistant cells. As depicted in Scheme 1, we postulated that the DSF released from PTX-DSF Ns would inactivate the P-gp-mediated drug efflux pump and thus sensitize drug-resistant tumor cells to a chemotherapeutic agent, PTX, ultimately enhancing apoptosis and therapeutic effects. Various *in vitro* proof-of-concept experiments were performed to study the potential effects of PTX-DSF Ns on reversing MDR in sensitive and Taxol-resistant A549 human lung adenocarcinoma cells, A549 and A549/TAX cells, respectively.

MATERIALS AND METHOD

Materials

PTX (99% purity) was purchased from Yew Biotechnology Co., Ltd. (Jiangsu, China). DSF ($\geq 97\%$ purity), bovine serum albumin (BSA), β -LG (90% purity), fluorescein 5(6)-isothiocyanate (FITC) (90% purity) and 3-(4, 5-dimethylthiazol-2-yl)-2, 5-diphenyltetrazolium bromide (MTT) (98% purity) were purchased from Sigma-Aldrich Co., Ltd. (St. Louis, MO, USA). The Annexin V-FITC/PI apoptosis detection kit was obtained from Nanjing KeyGen Biotech Co., Ltd. (Nanjing, China), the cell cycle assay kit was purchased from Solarbio Science & Technology Co., Ltd. (Beijing, China), and the caspase-3 and -9 calorimetric assay kit was obtained from Nanjing KeyGen Biotech Co., Ltd. (Nanjing, China). The BCA protein estimation kit was purchased from Beyotime Institute of Biotechnology Co., Ltd. (Haimen, China). The QuantiTect SYBR Green PCR kit was obtained from QIAGEN Inc. (Germantown, MD, USA). Human lung adenocarcinoma A549 cells were purchased from Nanjing



Scheme 1 (1) PTX-DSF NPs were prepared by antisolvent precipitation method. (2) PTX-DSF NPs enter resistant lung adenocarcinoma cells (A549/TAX) and deliver a synergistic concentration of PTX and DSF to the tumor cells. (3) Released DSF suppresses overexpressed MDR-1 associated P-gp efflux pump, subsequently (4) increases intracellular PTX concentration and finally (5) promotes apoptosis by initiating (6) caspase-3 and caspase-9 cascade and (7) G₂/M cell cycle phase arrest.

KeyGen Biotech Co., Ltd. (Nanjing, China) and Taxol-resistant A549/TAX cells were established in our lab using the dose escalation method. Fetal bovine serum (FBS) and RPMI-1640 cell culture medium were obtained from Wisent Inc. (St. Bruno, Quebec, Canada). PBS, trypsin-EDTA (more than 6000 U/mg) and a 100 U/ml penicillin+100 μ g/ml streptomycin solution were obtained from Nanjing KeyGen Biotech Co., Ltd. (Nanjing, China).

Preparation and Characterization

PTX-DSF NPs were prepared and β -LG was denatured using methods described in our previous report (25), with a few modifications. Briefly, 30 mg of β -LG was added to a tube containing 30 ml of distilled water to prepare a 1 mg/ml β -LG protein solution (antisolvent protein solution in water). After vigorous vortexing, stirring for 2 h at room temperature and

adjusting the pH to 7.0 using 0.1 M HCL or NaOH, the protein solution was heated to more than 90°C for 30 min. Then, the PTX-DSF Ns was prepared by using the antisolvent precipitation method. Briefly, 6 mg of PTX and 1 mg DSF were co-dissolved in 1 ml of organic solvent (acetone) to prepare 6:1 mg/ml dual drug solution. Then, 1 ml of the dual drug solution was poured into 10 ml of a 1 mg/ml protein solution (less than 4°C) with constant stirring. After antisolvent precipitation, formulations were immediately sonicated with an ultrasonic probe (20–25 kHz, Scientz Biotechnology Co., Ltd. Ningbo, China) at 600 W for 15 min. The duration of the ultrasonic burst was set to 3 s, with a pause of 4 s between two ultrasonic bursts. During ultrasonication, the temperature was controlled with an ice bath (4°C). Finally, PTX-DSF Ns were evaporated under reduced pressure with a rotating speed of 50 rpm at 25°C for 30 min to remove the residual acetone.

The FITC-PTX-DSF Ns or FITC-PTX Ns were prepared by co-dissolving FITC, DSF, and PTX in case of FITC-PTX-DSF Ns, while FITC and PTX for FITC-PTX Ns in acetone as an organic phase prior to use (26).

Particle Size, Polydispersity Index (PDI), and Zeta Potential

The particle size and PDI were measured according to the dynamic light scattering (DLS) principle using a 90Plus ZetaPlus Zeta Potential Analyzer (Brookhaven Instruments, Holtsville, NY, USA) at 25°C. The PDI was used as a measure of the particle size distribution. Raw data were collected over 5 min at 25°C and at an angle of 90°. The size was expressed as an intensity-weighted Gaussian distribution (with Chi-square value <3). The surface charge of the nanosuspensions was determined by measuring the electrophoretic mobility at 25°C. The sample was diluted 100-fold in water prior to the measurement.

Scanning Electron Microscopy (SEM) and Transmission Electron Microscopy (TEM)

The SEM test was performed on a Philips XL30 SEM (Eindhoven, Holland) at an excitation voltage of 10 kV. The diluted sample was placed on a brass stub and dried at 25°C. Then, the sample was coated with gold using a sputter coater for 180 s under a vacuum.

The TEM examination was conducted on a JEM-1230TEM (Tokyo, Japan) at an accelerated voltage of 200 kV. After a 200-fold dilution, one drop of sample was deposited on a copper mesh and dried at 25°C, followed by removing the excessive sample with filter paper. Next, one drop of 2% (*w/w*) phosphotungstic acid was added to stain the sample for 30 s. After removing the superfluous phosphotungstic acid, the sample was desiccated at 25°C for 5 min.

In Vitro Stability

In vitro colloidal stability was examined in high ionic strength solutions, including saline (0.9% NaCl, ionic strength 154 mM), phosphate buffer saline (PBS, pH 7.4, ionic strength 162.7 mM) and PBS containing 10% serum (pH 7.4), by measuring the particle size, PDI and zeta potential. The particle size, PDI and surface charge of samples were assayed at specific time points.

Powder X-Ray Diffraction (PXRD) Analysis

A PXRD examination was conducted on a D8 advance diffractometer (Bruker, Germany) over the 2.5–50° 2 θ range at a scan rate of 3°/min, where the tube anode was Cu with $K\alpha = 0.154$ nm monochromatized with a graphite crystal. The pattern was collected at a 40 kV tube voltage and 60 mA of tube current in step scan mode (step size 0.02°, counting time 1 s/step).

Fluorescence and Circular Dichroism (CD) Spectra

The fluorescence spectrum was investigated by scanning from 300 to 800 nm at an excitation wavelength of 295 nm using a fluorescence spectrometer (Shimadzu RF-5301 PC, Japan). Far (190–250 nm) and near (250–420 nm) CD spectra were recorded on J-810 spectrometer (Tokyo, Japan) equipped with a temperature controlling unit and a quartz cuvette to determine the secondary and tertiary structures of the native and denatured β -LG protein solution in water, as well as β -LG in PTX-DSF Ns with different drug-loading capacities, in which the β -LG concentration remained constant in each formulation. The ellipticity was expressed in millidegrees. The following parameters were used for CD examinations: wavelength, 190–420 nm; bandwidth, 1 nm; scanning speed, 100 nm/min; cell length, 0.1 cm; response, 1 s; temperature, 25°C; β -LG concentration, 0.15 mg/ml (pH 7.0). The samples used for the fluorescence spectroscopy analysis were same samples used to collect CD spectra, except the concentration of β -LG was 0.25 mg/ml (pH 7.0).

Drug Encapsulation Efficiency (EE%) and Drug Loading (DL%)

PTX-DSF Ns were incubated with 15 ml of a pepsin solution (5%) to digest the β -LG and break the nanoparticles for 12 h, diluted with 3 ml of diethyl ether and centrifuged at 10,000 g for 10 min to determine the EE% and DL%. Next, the supernatant was collected and analyzed using the high-performance liquid chromatography (HPLC) system (Shimadzu LC-10AT, Kyoto, Japan) described below. The EE% and DL% of PTX and DSF were calculated using following formulas:

EE(%) = Amount of drug encapsulated / Amount of drug added \times 100%

DL(%) = Amount of drug encapsulated / Amount of β -LG \times 100%

In Vitro Drug Release

The *in vitro* release test was performed at two different pH (pH 7.4 and 5.4) using the dialysis method and a 3.5 kDa molecular weight cutoff dialysis bag. Dialysis was performed in an incubator with a shaking speed of 100 rpm/min at 37°C. The release media were PBS with 1% (*w/v*) Tween-80 at pH 7.4 or 5.4. At predetermined time intervals, 2 ml of sample were withdrawn from the dialysis bag and replenished with the respective fresh release medium. Upon centrifugation at 15,000 g for 5 min, the concentrations of PTX and DSF in the supernatant were quantified using HPLC system equipped with an LC-10AT pump and SPD10A UV-detector (Shimadzu, Tokyo, Japan). PTX and DSF were separated on a Diamonsil C₁₈ column (4.6 mm \times 250 mm) at 227 and 275 nm, respectively. A mixture of methanol and water (80: 20, *v/v*) was used as the mobile phase with a flow rate of 1.0 ml/min at 37°C. The injection volume was 20 μ l.

Cell Culture

A549 and A549/TAX were cultured in RPMI-1640 supplemented with 10% FBS and 100 U/ml penicillin+100 μ g/ml streptomycin at 37°C in a 5% CO₂ humidified incubator (Thermo Scientific, Waltham, MA, USA).

Establishment of A549/TAX Cells

A549/TAX cells were obtained using the dose escalation method, as described in previous reports (27,28). Briefly, A549 cells in logarithmic growth phase were cultured in RPMI-1640 medium for 48 h. Next, cells that had reached 80% confluence were incubated with Taxol at a PTX concentration of 20 ng/ml for 24 h. Because Taxol induces apoptosis, sensitive cells died and then surviving cells were collected and cultured in Taxol-free culture medium until the next logarithmic phase. In the next cycle, cells were cultivated and Taxol induced apoptosis as described in the previous cycle until the Taxol concentration had increased from 20 ng/ml to 400 ng/ml in a gradient (20, 40, 60, 80, 100, 200, 300 and 400 ng/ml). The process was repeated until the A549 cells grew steadily in medium containing 400 ng/ml Taxol. At this stage, the A549 cells were A549/TAX cells. The fold resistance of A549/TAX cells was calculated by determining the half maximal inhibitory concentration (IC₅₀).

The drug resistance of A549/TAX cells was maintained by the addition of 100 ng/ml Taxol to the medium. Before

performing any cell-based experiment, A549/TAX cells were cultivated in Taxol-free culture medium for at least three days.

Cellular Uptake and Intracellular Tracking

A549 and A549/TAX cells were seeded in 24-well plates (1 \times 10⁵ cells/well) and incubated for 24 h at 37°C. Then, cells were treated with FITC-PTX-DSF Ns for 0.5, 1, 2, 4 and 8 h at 37°C at FITC concentrations ranging from 20 to 800 ng/ml in PBS (the mass ratio of PTX to DSF was 5:1). Next, cells were dissociated from the plates, collected, washed with PBS 3 times, and resuspended in 500 μ l of PBS. Finally, the fluorescence intensity was measured by flow cytometry (FACSCalibur, BD Biosciences, USA).

A549 and A549/TAX cells (1 \times 10⁵ cells) were seeded on glass bottom culture dish (10 mm²) with a cover and were incubated for 24 h at 37°C. Then, the cells were incubated with FITC-PTX-DSF Ns in cell culture medium at a fixed FITC concentration of 800 ng/ml for 1, 2 and 4 h (mass ratio of PTX to DSF was 5:1) to examine the cellular localization. Cells were washed with ice-cold PBS 3 times, fixed with 4% paraformaldehyde, incubated with fresh medium containing LysoTracker Red for 2 h, washed with PBS for 3 times, incubated with DAPI (0.2 μ g/ml) for 20 min, and rinsed with PBS for 3 times. Cells were subsequently observed under a confocal laser scanning microscope (CLSM, LSM700, Zeiss, Germany).

Efflux Inhibition Assay

Quantitative and qualitative drug efflux studies were performed. For the quantitative drug efflux analysis, A549/TAX cells were seeded in 24-well plates (1 \times 10⁵ cells/well) and cultured for 24 h at 37°C. Then, cells were treated with FITC-PTX Ns and FITC-PTX-DSF Ns for 12 h at a FITC concentration of 800 ng/ml (the mass ratio of PTX to DSF was 5:1). Next, cells were trypsinized, collected, washed with PBS 3 times, resuspended in 500 μ l of PBS, and finally subjected to fluorescence measurements using flow cytometry.

For the qualitative drug efflux assay, the cells were incubated with FITC-PTX Ns or FITC-PTX-DSF Ns at a FITC concentration of 800 ng/ml (the mass ratio of PTX to DSF was 5:1) for 12 h, fixed with 4% paraformaldehyde, treated with LysoTracker Red for 2 h and stained with DAPI (0.2 μ g/ml) for 20 min. Finally, the cells were visualized with CLSM.

Cytotoxicity, Apoptosis and Synergistic Effects

The cytotoxicity of A549 and A549/TAX cells was assessed using the MTT assay. Briefly, cells were seeded in 96-well plate (5 \times 10⁴ cells/well) and cultured for 24 h to allow the cells to attach to the surface. Cells were then incubated with

different formulations at different drug concentrations for 24 and 48 h. The mass ratio between PTX and DSF in the free-drug combination formulation and PTX-DSF Ns was fixed at 5:1. In this experiment, untreated cells were used as a control. Next, 20 μl of MTT solution in PBS (5 mg/ml) were added to the each well, followed by a 4-h incubation at 37°C and the addition of 150 μl of DMSO. Finally, the absorbance was determined at 490 nm using a spectrophotometer (Thermo Scientific Multiskan FC Microplate Photometer, Waltham, MA, USA). Using the same method, the cytotoxicity of β -LG and the blank solution used to dissolve free drugs and their combination was also determined. The IC_{50} values were calculated using GraphPad Prism 5.01 software (GraphPad Software Inc. La Jolla, CA, USA).

For the cellular apoptosis assay, A549 and A549/TAX cells were seeded in 6-well plate at a density of 5×10^5 cells/well and incubated for 24 h at 37°C. Then, cells were incubated with the different formulations for 48 h. For the quantitative assessment of cellular apoptosis, the treated cells were collected, washed with PBS 3 times and stained with the Annexin V-FITC/PI apoptosis detection kit at room temperature for 15 min in the dark. Next, the cells were analyzed by flow cytometry.

The synergistic interaction between PTX and DSF was calculated at a fixed mass ratio using the CI equation (29,30):

$$CI = \frac{D_1}{D_{x1}} + \frac{D_2}{D_{x2}}$$

Where D_{x1} and D_{x2} are PTX and DSF concentrations alone required to inhibit 50% of cell growth, respectively, and D_1 and D_2 are the PTX and DSF concentrations in the combination treatment that also inhibit 50% of cell growth. Notably, $CI < 1$, $CI = 1$ and $CI > 1$ indicated synergistic, additive and antagonistic effects, respectively. The CI and DRI were calculated using CompuSyn 1.0 software (ComboSyn, Inc., USA).

Mechanism of the Synergistic Effect

Cell Cycle Analysis

For the cell cycle analysis, A549 and A549/TAX cells were seeded in 6-well plates at a density of 5×10^6 cells/well and incubated for 24 h at 37°C. Then, cells were incubated with the different formulations for 48 h (the mass ratio of PTX to DSF was 5:1). The treated cells were then collected, washed with ice-cold PBS 3 times and fixed with 70% ethanol overnight at 4°C. Next, the cells were consecutively treated with RNase A and 5 $\mu\text{g}/\text{ml}$ PI for 30 min in the dark. Finally, the alterations in the cell cycle were analyzed by flow cytometry.

Caspase-3 and Caspase-9 Assay

Caspase-3 and caspase-9 assays were performed to explore the apoptosis mechanism. The assays were conducted using caspase-3 and -9 calorimetric assay kits, according to manufacturer instructions. Briefly, A549 and A549/TAX cells were seeded in 6-well plates (5×10^6 cells/well) and incubated for 24 h at 37°C. Then, cells were incubated with the different formulations for 48 h. Next, cells were washed with PBS 2 times and collected by centrifugation at 2000 rpm for 5 min. After removing the PBS, 200 μl of lysate buffer for the caspase-3 assay and 100 μl for the caspase-9 assay were added to the cells, incubated on ice for 20 min, vigorously vortexed for 10 s and centrifuged at 10,000 rpm at 4°C to collect the supernatant (cell lysate). The total protein concentration was measured using the BCA protein estimation kit. Caspase assays were performed by mixing 50 μl of cell lysate with 50 μl of $2 \times$ reaction buffers and 5 μl of caspase substrate and then incubating the mixture for 4 h in the dark at 37°C. Finally, the optical density of the reaction mixture was measured at 405 nm using a spectrophotometer (Thermo Scientific Multiskan FC Microplate Photometer, Waltham, MA, USA).

MDR-1 Gene Expression Assay

The analysis of MDR-1 expression was performed using RT-qPCR. Briefly, total RNA was extracted from A549 and A549/TAX cells using Trizol reagent, according to the manufacturer's instructions. The purity and concentration of RNA were estimated using a NanoDrop spectrophotometer (Thermo Scientific, MA, USA). Total RNA (1 μg) was used to synthesize cDNAs in a 20 μl reaction mixture on a Master Cycler Nexus GSX1 (Eppendorf, NY, USA) with the following 40 thermal cycles: 25°C for 5 min, 50°C for 15 min and 85°C for 5 min.

The RT-qPCR was performed in 20 μl reaction mixture of each sample in triplicate in 96-well plate and run on Quant Studio 3 Real-time qPCR (Applied Biosystems, CA, USA). The specific primers used to amplify the MDR-1 and β -actin cDNAs are shown in **Table SI**. Here, β -actin was used as housekeeping gene for normalization. In each reaction mixture, the primer and cDNA concentrations for each gene were 0.4 μl and 50 ng, respectively. The amplification cycle conditions were: 95°C for 5 min (pretreatment stage 1), 95°C for 10 s and 60°C for 30 s (cycling or reaction stage 2), 95°C for 15 s, 60°C for 1 min and 95°C for 15 s (melting curve stage 3) for a total of 35 thermal cycles. The expression level of the MDR-1 mRNA was normalized to β -actin expression, and relative mRNA levels were calculated by $2^{-\Delta\Delta\text{CT}}$ method (31). Finally, after amplification, the PCR products (10 μl) of each reaction were subjected to electrophoresis in a 2% agarose gel.

Statistical Analysis

All results are presented as means \pm SD, and each value was the mean of three replicate independent experiments performed in parallel. Statistical analyses were performed using the 2-way ANOVA test. All analysis are shown compared to the control and the significance of the difference is indicated as * $P < 0.05$, ** $P < 0.01$, or *** $P < 0.001$.

RESULTS

Preparation and Characterization

The present study was aimed to design a novel nanosuspension for the codelivery of PTX and DSF to overcome MDR and promote cytotoxicity in Taxol-resistant cells. Here, β -LG, which acted as a stabilizer, was used to coat the nanocrystals of PTX and DSF (PTX-DSF Ns) prepared using an antisolvent precipitation method. First, we optimized the formulations by increasing the concentration of PTX (1–10 mg) while maintaining the DSF concentration at a constant value (1 mg) or increasing the DSF concentration (0.1–1 mg)

while maintaining PTX concentration at a fixed concentration (6 mg). As displayed in Fig. S1, the smallest particle size, approximately 160 nm, was obtained from the combination of 6 mg:1 mg or 5 mg:1 mg of PTX and DSF. The former combination had a higher drug-loading capacity and a lower PDI value than the latter combination, and therefore, it was selected as the optimized formulation for the subsequent studies.

The PTX-DSF Ns prepared from the optimized formulation exhibited a slightly milky color but was transparent and homogeneous in physical appearance and had a hydrodynamic diameter, PDI and surface charge of 160 nm, 0.23 and approximately -24 mV, respectively (Fig. 1, panel A). The negative charge was due to the β -LG coating (32). SEM and TEM examinations confirmed that the PTX-DSF Ns showed a rod-like morphology with particle diameter of approximately 150 to 200 nm (Fig. 1, panels B and D). The freeze-dried PTX-DSF Ns exhibited incompact and porous features (Fig. 1, panels C and E); after redispersion in water, a considerable number of rod-like particles with a length of approximately 150 to 200 nm was observed (Fig. 1, panel E). Based on these results, PTX-DSF Ns was able to be freeze dried for long-term storage. Furthermore, according to the HPLC results,

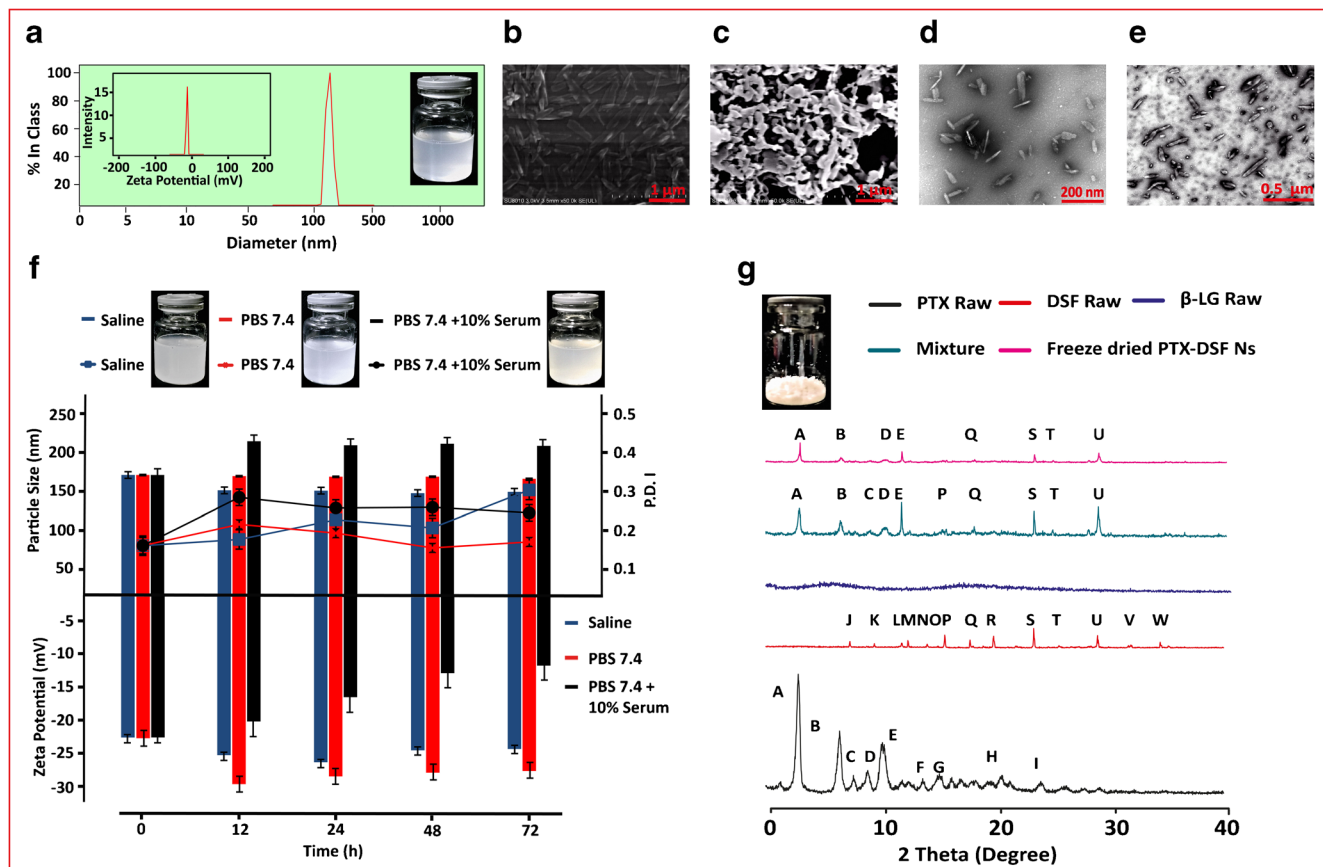


Fig. 1 Characterization. (a) Size distribution, zeta potential and an optical picture of PTX-DSF Ns. SEM images of (b) PTX-DSF Ns and (c) freeze dried sample. (d) TEM images of PTX-DSF Ns and (e) redispersed sample. (f) Physical stability. (g) PXRD assay.

the drug-loading capacities of PTX and DSF in the optimized formulation of PTX-DSF Ns were approximately $36.23 \pm 0.9\%$ with an EE% of $96.6 \pm 0.24\%$ and $7.38 \pm 0.12\%$ with an EE% of $81.2 \pm 1.35\%$, respectively. Based on subsequent calculations, the accurate mass ratio of PTX to DSF in PTX-DSF Ns was approximately 5:1. Surprisingly, the drug-loading capacity of the MDR modulator drug (DSF) was 3–6-fold greater than in the previously reported studies (33,34).

In Vitro Stability

The stability of PTX-DSF Ns regarding particle size and PDI was examined in three different solutions: saline, PBS pH 7.4 (high ionic strength solution) and PBS pH 7.4 supplemented with 10% FBS (physiological fluid). The particle size in saline decreased from 162 nm to 140 nm, whereas the PDI was increased from 0.13 to 0.28 over time. No noticeable changes in these two parameters were observed in PBS pH 7.4. In PBS pH 7.4 + 10% FBS, the particle size and PDI of PTX-DSF Ns increased from 162 to 202 nm and from 0.13 to 0.22, respectively (Fig. 1, panel F), owing to protein absorption.

Zeta potential is also an important parameter that determines the physical stability of nanoparticles. The zeta-potential values of PTX-DSF Ns were changed from -22 to -23 mV and -22 to -27 mV in saline and PBS pH 7.4 medium, respectively. In PBS pH 7.4 + 10% FBS, the zeta potential varied significantly from -22 to -10 mV at the end of study period (Fig. 1, panel F).

PXRD Analysis

As shown in Fig. 1, panel G, PTX showed three intense peaks (A, B, and E) at 2θ equal to 5.68° , 8.96° and 12.42° , and DSF showed four characteristic peaks (O, R, S, and U) at 17.05° , 21.46° , 24.68° and 29.82° . In contrast, no characteristic peaks were observed for β -LG, whereas the physical mixture displayed five peaks (A, B, E, S, and U) at 5.68° , 9.06° , 13.88° , 24.54° , and 29.72° , respectively. For PTX-DSF Ns, four characteristic peaks (A, B, S, and U) at 5.74° , 13.92° , 24.58° and 29.76° were observed. The freeze dried PTX-DSF Ns powder exhibited major diffraction peaks for both PTX (A and E) and DSF (S and U), although the intensity of the peaks was not as high as the raw powders. Thus, PTX and DSF were mainly present as microcrystals in PTX-DSF Ns.

Fluorescence and CD Spectra

Fluorescence spectroscopy is a potent tool used to study the structure and conformational changes in proteins (35,36). The emission characteristics of tyrosine, phenylalanine, and tryptophan (Trp) residues present in many proteins have been proven to be quite handy in understanding the binding

mechanisms and conformational changes in proteins upon interactions with membranes (37), small molecules (38,39) and nanoparticles (40–43). In this study, the interaction between β -LG and the cocrystals of PTX and DSF was investigated using fluorescence spectroscopy. β -LG contains two Trp residues with intrinsic fluorescence; however, fluorescence quenching occurs as the local hydrophobic environment of the Trp residue is disrupted. The effects of heat-induced denaturation and drug-loading capacity on the fluorescence quenching of β -LG are shown in Fig. 2, panels A and B. A significant decrease in fluorescence intensity was observed for denatured β -LG compared with the native protein, indicating that the heat-induced denaturation exposed the Trp residues in the protein to less hydrophobic conditions. Specifically, the incorporation of cocrystals (the mass ratio of PTX to DSF was 5:1) into the denatured β -LG solution significantly quenched the fluorescence, followed by a red shift of λ_{max} from 353 to 359 nm, regardless of the difference in drug-loadings, indicating robust interactions between them. Interestingly, the maximum intensity increased as the drug-loading capacity increased, and in particular, the intensity markedly increased as the drug-loading capacity increased to 5 mg:1 mg of PTX: DSF. At low drug-loading capacities, the drug tended to interact with the protein, subsequently forming protein-drug complexes that ultimately assembled into nanocomplexes and re-established a hydrophobic environment for the Trp residues. In contrast, at high drug-loading capacities, the protein tended to absorb on the hydrophobic surface of drug particles and thus allowed the Trp residues to be trapped in a more hydrophobic environment (18).

CD spectroscopy was performed to further understand the interaction between the cocrystals with β -LG. CD spectroscopy is a very sensitive and comprehensive tool used to monitor the alterations in secondary and tertiary structures in proteins induced by guest molecules. Figure 2, panels C-F shows the far and near UV-CD spectra of native and denatured β -LG and the effects of drug-loading capacity on the denatured β -LG. The far CD spectra of native and denatured β -LG exhibit a β -sheet structure and α -helix with a wide negative minimum at λ_{max} 218 nm; however, the denatured β -LG exhibited a decrease in the negative minimum and therefore displayed decreased α -helical contents after heat-induced denaturation (Fig. 2, panels C and E). The near CD spectra also showed a positive peak for native β -LG at approximately 360 nm and a negative peak at λ_{max} 353 nm for denatured β -LG. Based on these changes, the heating process induced conformational changes in the secondary and tertiary structures of β -LG (44). Importantly, the drug-loading capacity of PTX and DSF (mass ratio of PTX to DSF was 5:1) significantly influenced the CD spectra of denatured β -LG. In detail, as the drug-loading capacity increased from 0 to 36 mg (30 mg:6 mg of PTX: DSF), the negative minimum decreased, with a red shift of λ_{max} from 218 nm to 236 nm in far CD spectra, and the

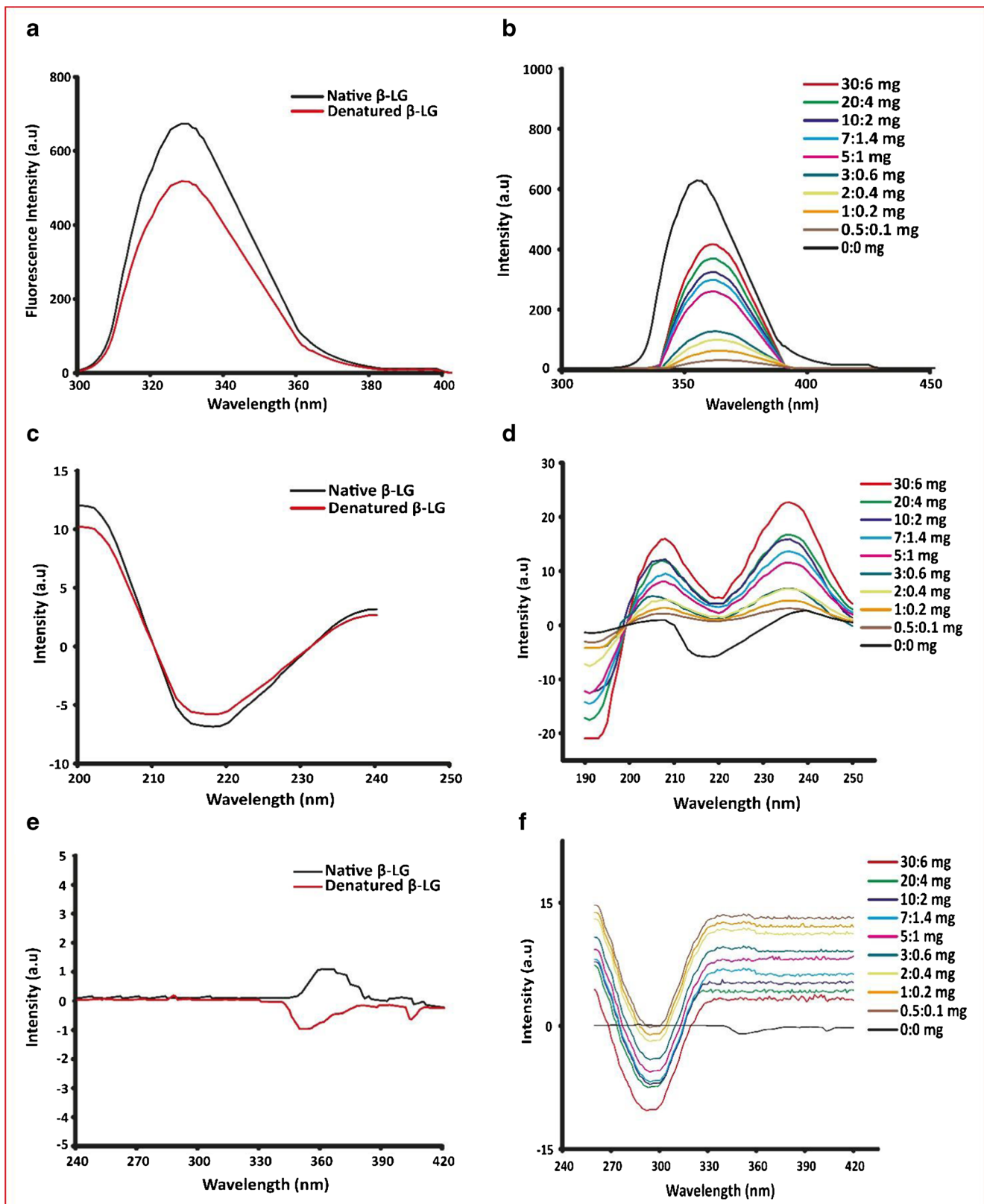


Fig. 2 Fluorescence emission spectra of (a) native and denatured β -LG, (b) different drug combination ratio of PTX-DSF Ns. (c) Far and (e) near UV-CD of native and denatured β -LG, (d) far and (f) near UV-CD of different drug combination ratio of PTX-DSF Ns. The β -LG concentration in the aqueous phase was 0.25 and 0.15 mg/ml for fluorescence spectrum and CD examination, respectively.

negative minimum increased, with a red shift of λ_{max} from 351 to 337 nm in near CD spectra (Fig. 2, panels D and F). Nonetheless, these changes spanning low and high drug-loading capacities were different due to the formation of different nanoformulations and subsequent placement of the intrinsic fluorescent residues of the protein in a new environment, consistent with the fluorescence spectra. Collectively, these data revealed alterations in the secondary and tertiary structures of denatured β -LG induced by the cocrystals and thus verified a robust interaction between the two.

In Vitro Drug Release

The *in vitro* drug release profile of PTX-DSF Ns was evaluated to examine whether the DSF would be temporally released in a sustainable manner to achieve constant inactivation of the P-gp drug efflux pump, as well as to observe the release behavior of PTX from PTX-DSF Ns after cellular uptake. As shown in Fig. 3, panels A and B, approximately 68% and 83% of DSF were released from PTX-DSF Ns at 12 h at pH 7.4 and 5.4, respectively, with an initial burst of 54% at pH 7.4 and 60% at pH 5.4 within 1 h. Furthermore, at 48 h, approximately 70% and 88% of DSF were released at pH 7.4 and 5.4, respectively. In contrast, more than 90% of DSF was released from raw DSF particles at 1 h. At 12 h, 68% and 83% of PTX were released from PTX-DSF Ns, with an initial burst of 18% and 30% in the first 1 h at pH 7.4 and 5.4, respectively. Moreover, approximately 78% and 96% PTX were released at 48 h at pH 7.4 and 5.4, respectively. Similarly, PTX release from raw particles displayed a very fast pattern, with complete release observed at 1 h. Thus, the β -LG coating on the cocrystals delayed the drug release, although smaller sized particles have an increased surface for release. The following reasons may contribute to this result. Initially, the protein coating may limit the drug diffusion into the release media. Second, the interplay between the drug and protein and the subsequent formation of protein-drug complexes slowed the release (45).

Overall, the fast and sustained kinetics of DSF release from PTX-DSF Ns will guarantee the swift and constant suppression of the P-gp drug efflux pump, ultimately reversing MDR. PTX release kinetics showed that an efficient level of PTX would be available to induce the apoptosis of cancer cells after cellular uptake.

Cellular Uptake and Intracellular Tracking

The levels of MDR-1 in A549 cells post-treated with Taxol were assayed by RT-qPCR and gel electrophoresis to ascertain the establishment of the Taxol-resistant A549 cell line (A549/TAX cells). As depicted in Fig. S2, panels A and B, A549/TAX cells expressed 2.2-fold higher levels of the MDR-1 than parent A549 cells, which was confirmed by gel electrophoresis showing that a bright band for the MDR-1 was observed in A549/TAX cells. Thus, A549/TAX cells had a significant ability to resist Taxol and were used in subsequent studies.

For the quantitative measurement of cellular uptake in A549/TAX and A549 cells, cells were incubated with FITC-PTX-DSF Ns. In general, the cellular uptake of FITC-PTX-DSF Ns occurred in a time- and concentration-dependent manner in the two cell lines (Fig. 4, panels A and B). In contrast, the uptake of nanoparticles in A549/TAX cells was much higher than that in A549 cells due to the inactivation of P-gp drug efflux pump.

After treatment with FITC-PTX-DSF Ns, the cells were observed by CLSM (Fig. 4, panels C and D). The intracellular green fluorescence around the nucleus in A549 cells became stronger over time. In contrast, the green fluorescence in A549/TAX cells at 1 h or 2 h was more robust than that at 4 h. In both cell lines, when LysoTracker red-labeled lysosomes and green fluorescent FITC-PTX-DSF Ns were merged, a yellow color appeared, indicating that FITC-PTX-DSF Ns were located in lysosomes and that the cellular uptake occurred through the endo-lysosomal pathway. Again,

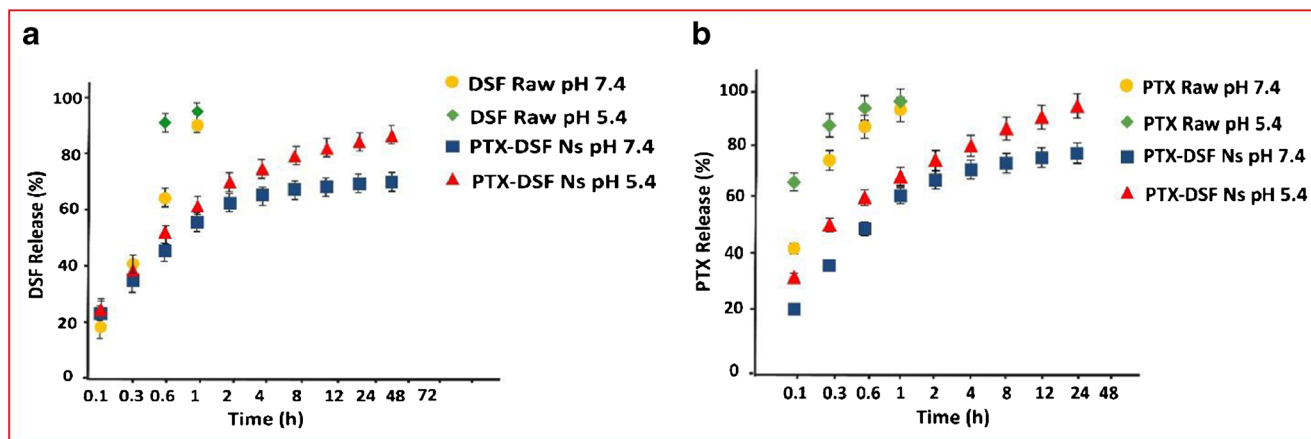


Fig. 3 *In vitro* release profiles of (a) DSF and (b) PTX from raw particles or PTX-DSF Ns in pH 5.4 or pH 7.4 media containing 1% Tween-80 at 37°C.

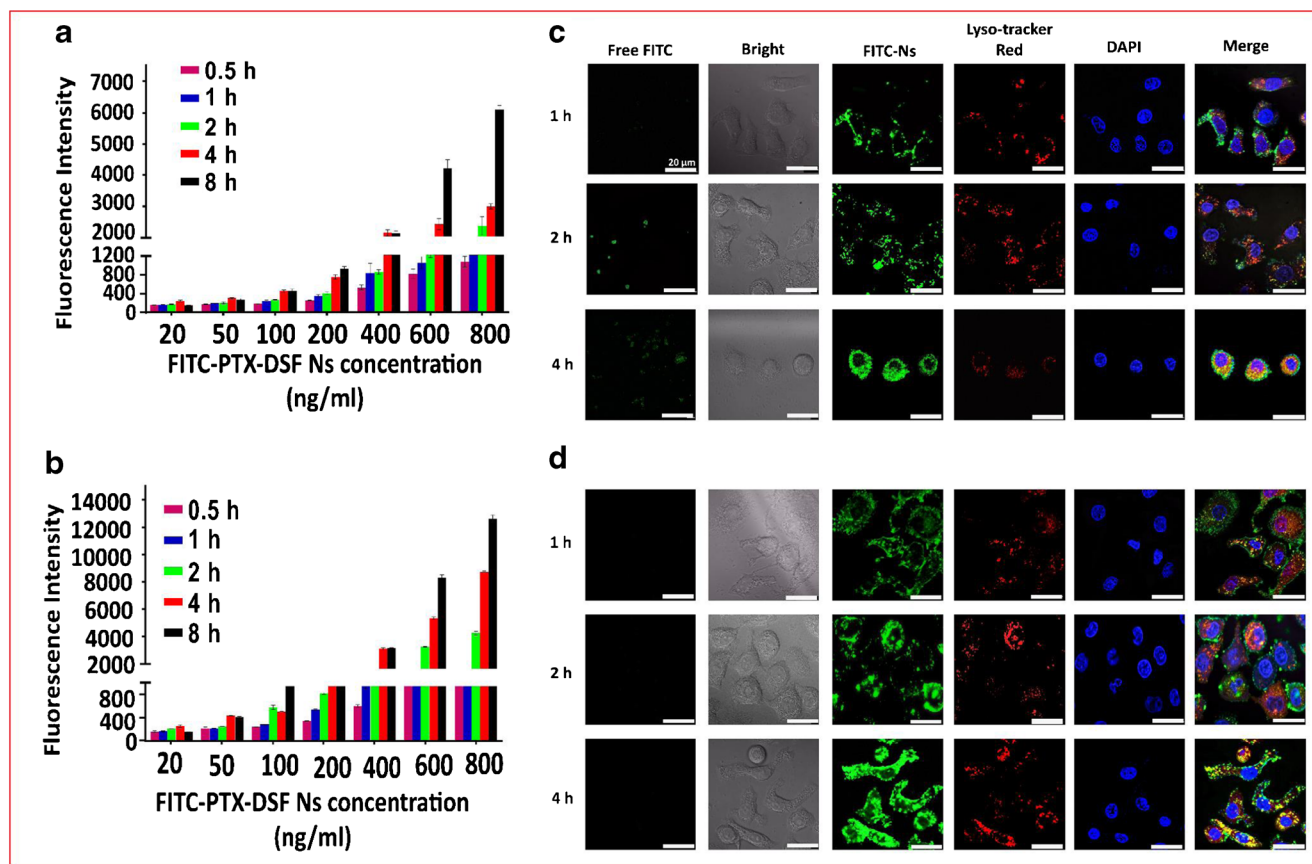


Fig. 4 Flow cytometry analysis of cellular uptake of FITC-PTX-DSF Ns in (a) A549 and (b) A549/TAX at different concentrations of FITC after incubation for different durations. CLSM images of (c) A549 and (d) A549/TAX cells treated with FITC-PTX-DSF Ns for different durations at fixed FITC concentration of 800 ng/ml. Scale bar: 20 μ m.

at initial time points (1 h and 2 h), the intracellular accumulation of FITC-PTX-DSF Ns in A549/TAX cells was significantly greater than that in A549 cells. Taken together, the intracellular accumulation of PTX-DSF Ns in A549/TAX cells was markedly improved compared with that in A549 cells.

Efflux Inhibition Assay

DSF downregulates P-gp expression by covalently altering the cysteine residues within the nucleotide binding region, which leads to the higher cellular uptake of cytotoxic drugs (46). A drug efflux assay was performed to further verify that the inactivation of P-gp by DSF enabled higher uptake of FITC-PTX-DSF Ns in A549/TAX cells. In this study, two types of nanoparticles, FITC-PTX Ns and FITC-PTX-DSF Ns, were formulated. As depicted in Fig. 5, panel A, the uptake of FITC-PTX Ns was initially time-dependent, and the maximum fluorescence intensity was observed at 8 h, but the intensity then unexpectedly decreased. On the other hand, FITC-PTX-DSF Ns showed a significant increase in fluorescence intensity in a time-dependent manner and peaked at 12 h, with no decline. The cellular uptake of FITC-PTX-

DSF Ns at 8 and 12 h was approximately 2-fold and 14-fold greater than that of FITC-PTX Ns.

A549/TAX cells were further examined by CLSM (Fig. 5, panel B). Interestingly, FITC-PTX Ns-treated cells showed lower intracellular and extracellular green fluorescence; in contrast, FITC-PTX-DSF Ns-treated cells displayed visible intracellular green and yellow fluorescence. Based on these findings, we concluded that: (i) A549/TAX cells overexpressed P-gp and therefore expelled FITC-PTX Ns, which was visualized as extracellular green fluorescence; (ii) DSF from FITC-PTX-DSF Ns successfully inactivated P-gp in A549/TAX cells, allowing for significant intracellular accumulation of FITC-PTX-DSF Ns over time.

Cytotoxicity, Apoptosis and Synergistic Effects

We first examined the cytotoxicity of β -LG and a blank cocktail solution (used to prepare the free-drug formulation) toward both cell lines (A549 and A549/TAX). No obvious cytotoxicity was observed even at high β -LG concentrations (Fig. S3).

A549 and A549/Tax cells were treated with different free-drug combinations (PTX-DSF mass ratios of 1:1, 3:1, 5:1 and

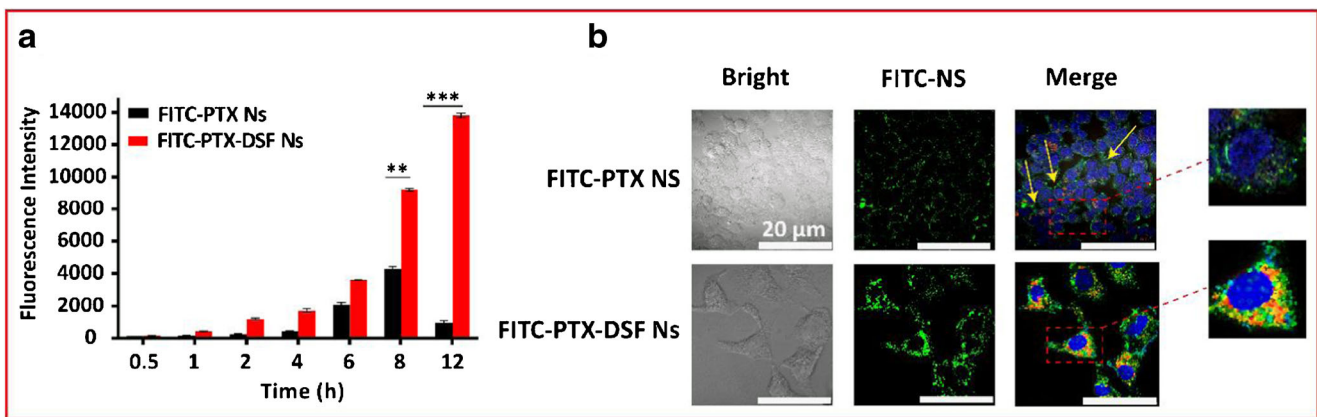


Fig. 5 (a) Cellular uptake of FITC-PTX Ns and FITC-PTX-DSF Ns in A549/TAX cells assayed by flow cytometry. (b) CLSM images of A549/TAX cells treated with FITC-PTX-DSF Ns or FITC-PTX Ns for 12 h at a fixed FITC concentration of 800 ng/ml. Scale bar: 20 μ m.

10:1) for 24 or 48 h and then the combination index (CI) and dose reduction index (DRI) were calculated, which a smaller value of CI indicates a better synergistic effect. The lowest CI values, including IC_{25} , 35, 50, 65, 75 and 90, were observed for the 5:1 ratio (Fig. S5 and S6, panels A-D) for A549/TAX cells. Moreover, the DRI for the ratio exhibited an approximately 1-fold and 2-fold increase compared with the other ratios in these two cell lines (Fig. S5, and S6 panels E and F), respectively. Based on these results, the 5:1 ratio of the free-drug combination promoted the synergy between the two drugs. Accordingly, a mass ratio of PTX-DSF of 5:1 was selected for further cytotoxicity study.

As displayed in Fig. S4, panels A-D, all formulations exhibited dose-dependent cytotoxicity. In general, the viability decreased as the drug concentrations increased from 0.1 to 100 μ g/ml of PTX. Compared with a single drug, the free-drug combination (PTX-DSF) and PTX-DSF Ns induced more substantial toxicity in A549 cells (Fig. S4, panels A and B), particularly in A549/Tax cells, indicating the synergistic effect. Critically, the viability of cells treated with PTX-DSF Ns was significantly lower than that treated with PTX-DSF. In particular, PTX-DSF Ns induced the apoptosis of A549/TAX cells (Fig. S4, panels C and D) at a greater efficiency than PTX-DSF, indicating a potent antitumor efficiency *in vitro*.

IC_{50} values were calculated based on the PTX concentration to ascertain the advantage of PTX-DSF Ns (5:1) compared to PTX-DSF and are shown in Table I. In A549 cells, PTX-DSF and PTX-DSF Ns decreased the IC_{50} values by >2-fold and 6-fold, respectively, compared with PTX. While, for A549/TAX cells, IC_{50} values for PTX-DSF and PTX-DSF Ns were reduced by 2.2/4.4-fold and 6/8-fold after 24 h/48 h incubation, respectively, compared with PTX. These data revealed the competent synergistic effect of the two drugs. Most importantly, PTX-DSF Ns (with a mass ratio of PTX/DSF of 5:1) achieved IC_{50} values of 1.82 and 2.08 μ g/ml for A549 cells after a 24-h and 48-h incubation, respectively, whereas the IC_{50} values for A549/TAX cells

were 2.03 and 1.82 μ g/ml after a 24-h and 48-h incubation, respectively. In contrast, at 24 and 48 h after treatment, PTX-DSF exhibited IC_{50} values of 3.82 and 3.24 μ g/ml for A549 cells and 4.65 and 3.17 μ g/ml for A549/TAX cells, respectively. According to a further comparative calculation, the PTX dose in PTX-DSF Ns required to generate the IC_{50} value was 1-fold lower than PTX-DSF, indicating a significantly enhanced synergistic effect of PTX-DSF Ns.

The CI for PTX-DSF Ns was calculated to validate the hypothesis that better synergy occurred between PTX and DSF in PTX-DSF Ns in A549/TAX cells. The CI values for PTX-DSF Ns at the IC_{50} for A549 cells were 0.206 and 0.335 at 24 h and 48 h after incubation, whereas the CI values for A549/TAX cells were 0.193 and 0.113 at 24 h and 48 h, respectively (Fig. 6, panels A and B). We also calculated CI values at IC_{25} , 35, 50, 65, 75 and 90, which were also in the synergistic range ($CI \leq 1$), and observed synergism at all inhibitory concentrations (IC). Importantly, these CI values for A549/TAX cells were less than the values for A549 cells and the DRI values for A549/TAX cells were markedly increased compared with A549 cells. Based on these data, PTX-DSF Ns achieved both synergism and a very promising PTX dose reduction; thus the PTX-DSF Ns have the potential to lower the systemic toxicity of the anticancer drug.

Table I IC_{50} (μ g/ml) Values for A549 and A549/Tax Cells After Treatment with Different Formulations for 24 or 48 h ($n = 3$)

Formulation	A549		A549/Tax	
	24 h	48 h	24 h	48 h
PTX	12.59 \pm 2.03	11.78 \pm 0.91	14.97 \pm 2.35	16.90 \pm 0.49
DSF	40.27 \pm 2.73	23.28 \pm 3.12	49.48 \pm 4.99	70.50 \pm 1.48
PTX-DSF	3.82 \pm 0.13	3.24 \pm 0.11	4.65 \pm 0.08	3.17 \pm 0.06
PTX-DSF Ns	1.82 \pm 0.11	2.08 \pm 0.41	2.13 \pm 0.15	1.82 \pm 0.28

^a IC_{50} Half maximum inhibitory concentration

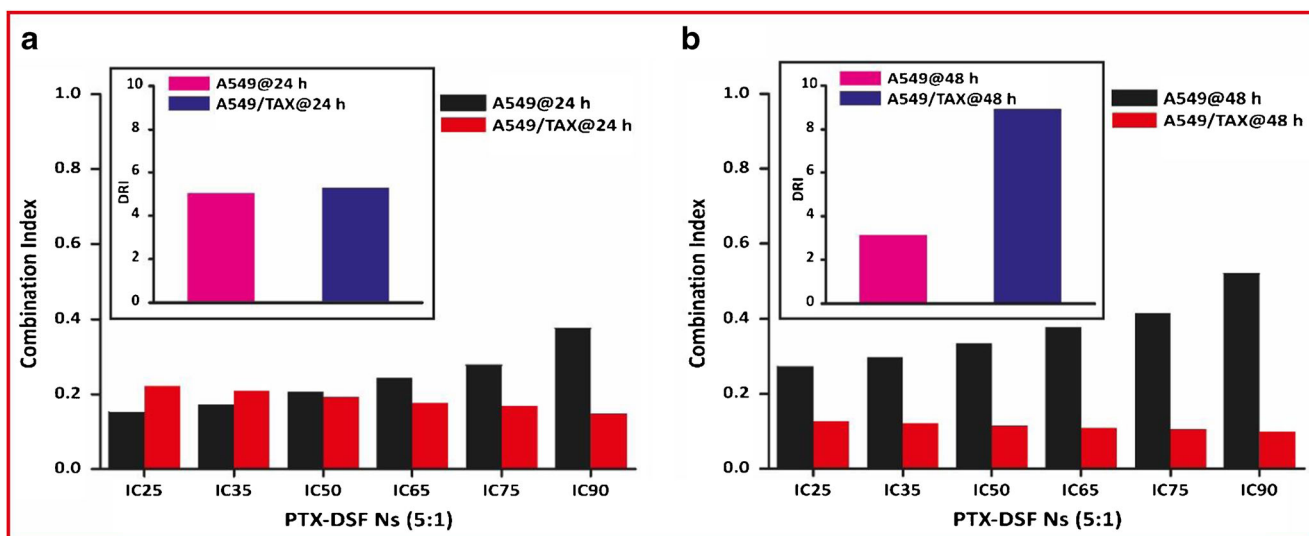


Fig. 6 Combination index (CI) for A549 and A549/TAX cells treated with PTX-DSF Ns (5:1) for (a) 24 h or (b) 48 h. CI < 1, CI = 1 and CI > 1 indicate synergistic, additive and antagonistic effects, respectively. The inset shows the dose reduction index (DRI) for PTX.

An Annexin V-FITC/PI staining assay was performed and both apoptotic and necrotic cells were quantified by flow cytometry to analyze apoptosis in A549 and A549/TAX cells. In A549 cells, both PTX-DSF and PTX-DSF Ns induced apoptosis in a significantly higher percentage than the single drugs; however, the total percentage of apoptotic cells induced by the two formulations was similar at approximately 77%. In contrast, the two formulations combining PTX and DSF induced a marked increase in the percentage of apoptotic A549/TAX cells compared with single drugs, however, PTX-DSF Ns induced 80% apoptosis while PTX-DSF induced 48% apoptosis (Fig. 7, panels A and B). Interestingly, the administration of DSF alone also induced apoptosis in both cell lines to some extent (33,47), indicating the potential anticancer activity of DSF, which requires further exploration.

Mechanism of the Synergistic Effect

Cell Cycle Analysis

The chemotherapeutic agent PTX interrupts the dynamic instability of microtubules required for cell division, thus causing cell cycle arrest and promoting the death of rapidly dividing cancer cells (48). A cell cycle analysis was performed to estimate the effects of PTX-DSF Ns on the cell cycle of A549 and A549/TAX cells (Fig. 8, panels A and B). In both cell lines, PTX predominantly generated cytotoxicity by decreasing and increasing the percentage of cells in G0/G1 and G2/M phases, respectively. In addition, the DSF treatment significantly reduced the percentage of A549 cells in G0/G1 phase, increased the percentage in G2/M phase, and subsequently displayed a certain amount of cytotoxicity. The combined formulations PTX-DSF and PTX-DSF Ns further increased the percentage of A549 cells in G2/M phase compared with

free PTX. Importantly, treatment with PTX-DSF or PTX-DSF Ns resulted in more substantial reduction in the percentage of A549/TAX cells in G0/G1 phase (6%) and an increase in the percentage of cells in G2/M phase (50%) compared with free PTX (16% and 35%, respectively), indicating their enhanced efficiency. By further reducing the percentage of cells in G0/G1 phase and increasing the percentage of cells in G2/M phase, the combination of PTX and DSF generated potent cytotoxic effects on A549 cells, particularly Taxol-resistant cancer cells.

Caspase-3 and Caspase-9 Assay

Caspase-3 and caspase-9 assays were performed on both A549 and A549/TAX cells after incubation to determine the underlying apoptosis mechanism. These data are shown in Fig. 9, panels A and B. In A549 cells, caspase-3 expression was upregulated by the combined formulations of PTX-DSF and PTX-DSF Ns compared with PTX, and caspase-9 expression was increased by PTX-DSF Ns. A similar increase of caspase-3 expression was observed in A549/TAX cells treated with PTX-DSF or PTX-DSF Ns; meanwhile, PTX-DSF Ns increased caspase-9 expression, but PTX-DSF did not. PTX-DSF Ns promoted caspase-3 and -9 expressions to a greater extent than PTX-DSF, and potentially enhanced the apoptosis and synergistic effect of the two drugs.

MDR-1 Gene Expression Assay

P-gp is encoded by the MDR-1 in multidrug-resistant cells (49). In this study, the expression of the MDR-1 in A549/TAX cells treated with different formulations was assayed by RT-qPCR and gel electrophoresis. As depicted in Fig. 9, panels C and D. The PTX treatment had little impact on

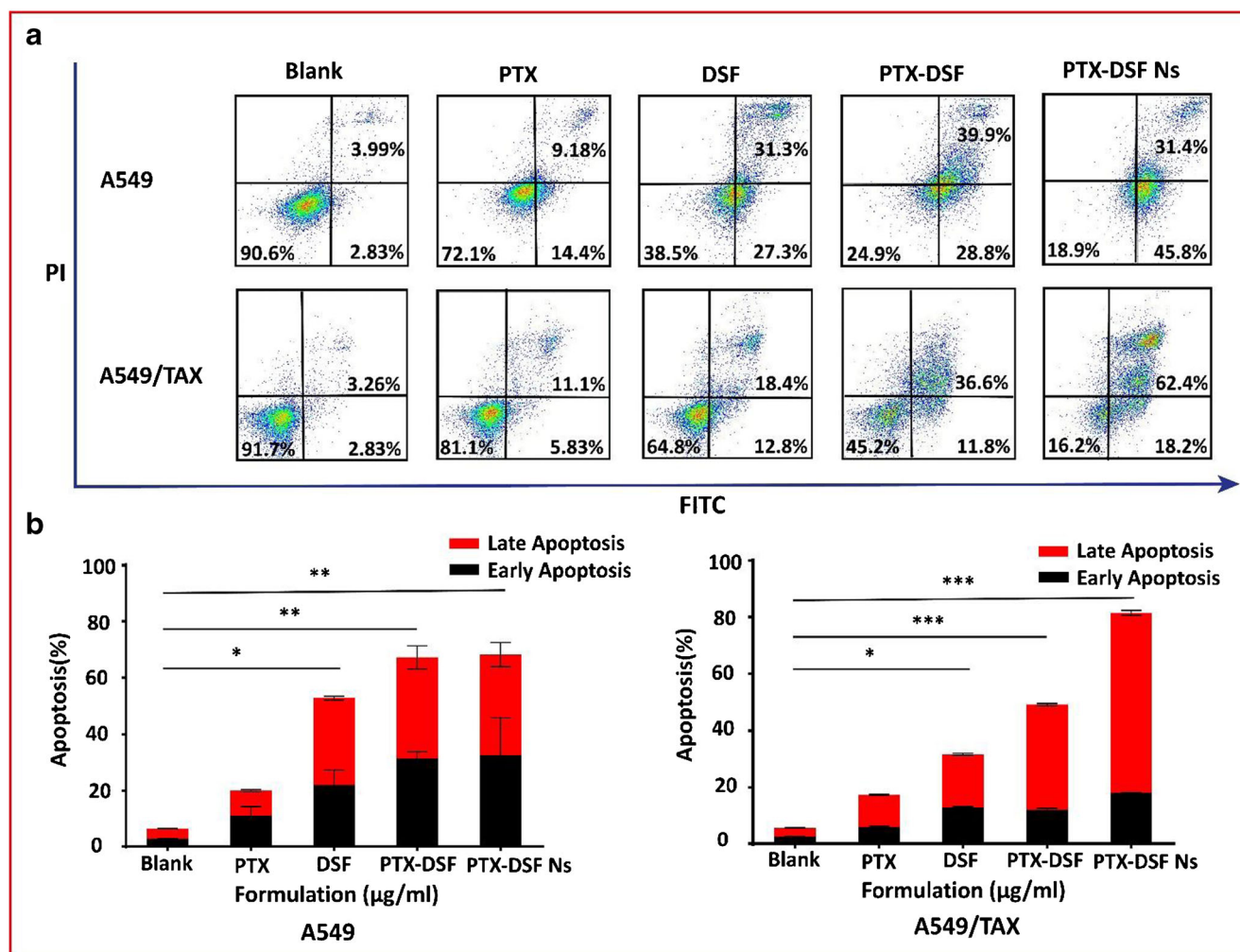


Fig. 7 (a) Flow cytometry analysis for apoptosis in A549 and A549/TAX cells after treatment with different formulation at a PTX or DSF concentration of 5 $\mu\text{g/ml}$ for 48 h at 37°C. (b) Quantitative assay of early and late apoptosis in A549 and A549/TAX cells. The mass ratio for PTX-DSF and PTX-DSF Ns was 5:1. $n = 3$, * $P < 0.05$, ** $P < 0.01$, and *** $P < 0.001$.

MDR-1 expression. In contrast, DSF, PTX-DSF and PTX-DSF Ns downregulated the MDR-1 expression by approximately 1-fold, 1-fold and 2.4-fold, respectively, compared with PTX. Interestingly, PTX-DSF Ns decreased the MDR-1 expression by 1.4-fold compared with PTX-DSF, again revealing their enhanced synergistic effect. Based on these results, DSF indeed downregulated the MDR-1 expression in A549/TAX cells, and PTX-DSF Ns further improved this inhibitory effect.

DISCUSSION

Nanosuspensions are a promising approach to address the solubility and bioavailability of insoluble drugs and reduce their side effects. Currently, more than 10 nanosuspension products have been launched in the market, indicating their great potential in clinical applications (17). Consequently,

nanosuspension products have attracted the attention of a large number of researchers interested in examining their *in vivo* fate (50), endocytic pathway for cellular entry (51), surface decoration for enhancing targeted delivery to the disease site (52), etc. On the other hand, pure drug nanoparticles in nanosuspensions undoubtedly belong to a type of nanoparticles, such as liposomes, micelles or nanocapsules, which have been employed as carriers for drug delivery. Unfortunately, the reported nanosuspensions only focus on the therapeutic effects instead of the carrier function that serves the drug delivery. Here, we present a nanosuspension coloaded with PTX and DSF, in which two drugs coprecipitate together to form cocrystals. Using β -LG as the stabilizer, the two drugs were incorporated into the particles, achieving codelivery of PTX and DSF. The stability of these PTX-DSF Ns was improved by the β -LG coating (a globular protein) via hydrophobic interactions between the drugs and coating protein. Few reports demonstrated that nanosuspensions can serve as carriers for

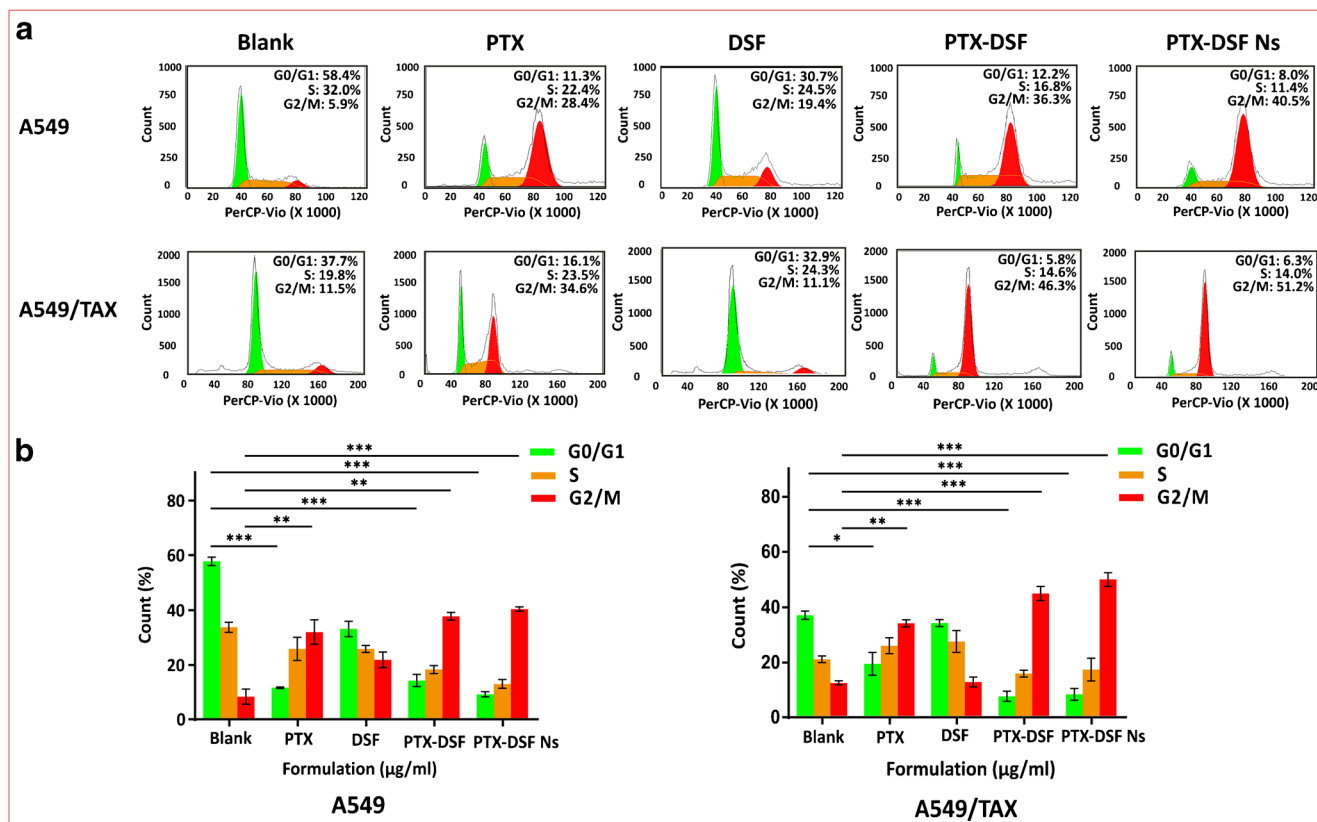


Fig. 8 (a) Cell cycle arrest and (b) cell cycle phase distribution of A549 and A549/TAX cells after treatment with different formulations at a PTX or DSF concentration of 5 $\mu\text{g/ml}$ for 48 h at 37°C. The mass ratio for combination of free PTX and DSF (PTX-DSF) and PTX-DSF Ns was 5:1. $n = 3$, * $P < 0.05$, ** $P < 0.01$, and *** $P < 0.001$.

codelivery. The conventional carriers for codelivery have low drug-loading capacity, thus reducing the therapeutic effect (14); moreover, this low capacity is shared by two drugs, further discounting the treatment. In contrast, the total drug-loading capacity of the present PTX-DSF Ns is approximately 43% (drug percentage compared to the weight of stabilizer), and the loadings of PTX and DSF are 36% and 7%, respectively; therefore, this formulation possesses promising potential to improve therapeutic outcomes. Moreover, the ratio of the combined chemotherapeutics is essential for the efficacy of the combination treatment, because the ratio of two drugs determines the possibility of synergism and antagonism of a combinatorial formulation (53). Accordingly, the mass ratio of two drugs in combined carriers should be precisely controlled or tuned (54). The precise control of both drugs in conventional carriers is poor, due to their low drug-loading capacity and the use of a complicated process for their preparation. Here, accurately tuning the mass ratio of both drugs in PTX-DSF Ns was easily achieved due to the simple preparation process, further implying the potential increased potency of nanosuspensions in the combined treatment.

DSF is an efficient MDR modulator that inhibits efflux and therefore markedly increases the accumulation of nanoparticles in Taxol-resistant cells. The uptake of FITC-PTX-DSF Ns in A549/TAX cells at 8 and 12 h post-incubation was 2-folds and 14-folds higher than FITC-PTX Ns; in particular, FITC-PTX Ns were almost completely exported at 12 h post-incubation (Fig. 5). Thus, DSF played a vital role in the enhanced uptake of nanoparticles in Taxol-resistant cells. Furthermore, based on the results of the MDR-1 assay, DSF in FITC-PTX-DSF Ns reduced MDR-1 expression more than 2-fold in Taxol-resistant cells compared with controls; in addition, the administration of DSF alone decreased the MDR-1 expression by 1-fold compared with the controls (Fig. 9). P-gp is encoded by the MDR-1. Therefore, by downregulating the MDR-1 expression and inactivating the P-gp pump, DSF increased the uptake of nanoparticles in A549/TAX cells. Moreover, the MDR reversal induced by DSF was significantly enhanced when DSF was encapsulated with PTX in nanoparticles. In fact, P-gp-mediated drug efflux is a common barrier to cancer chemotherapy and other disease treatments (55) as well as oral absorption (56). This

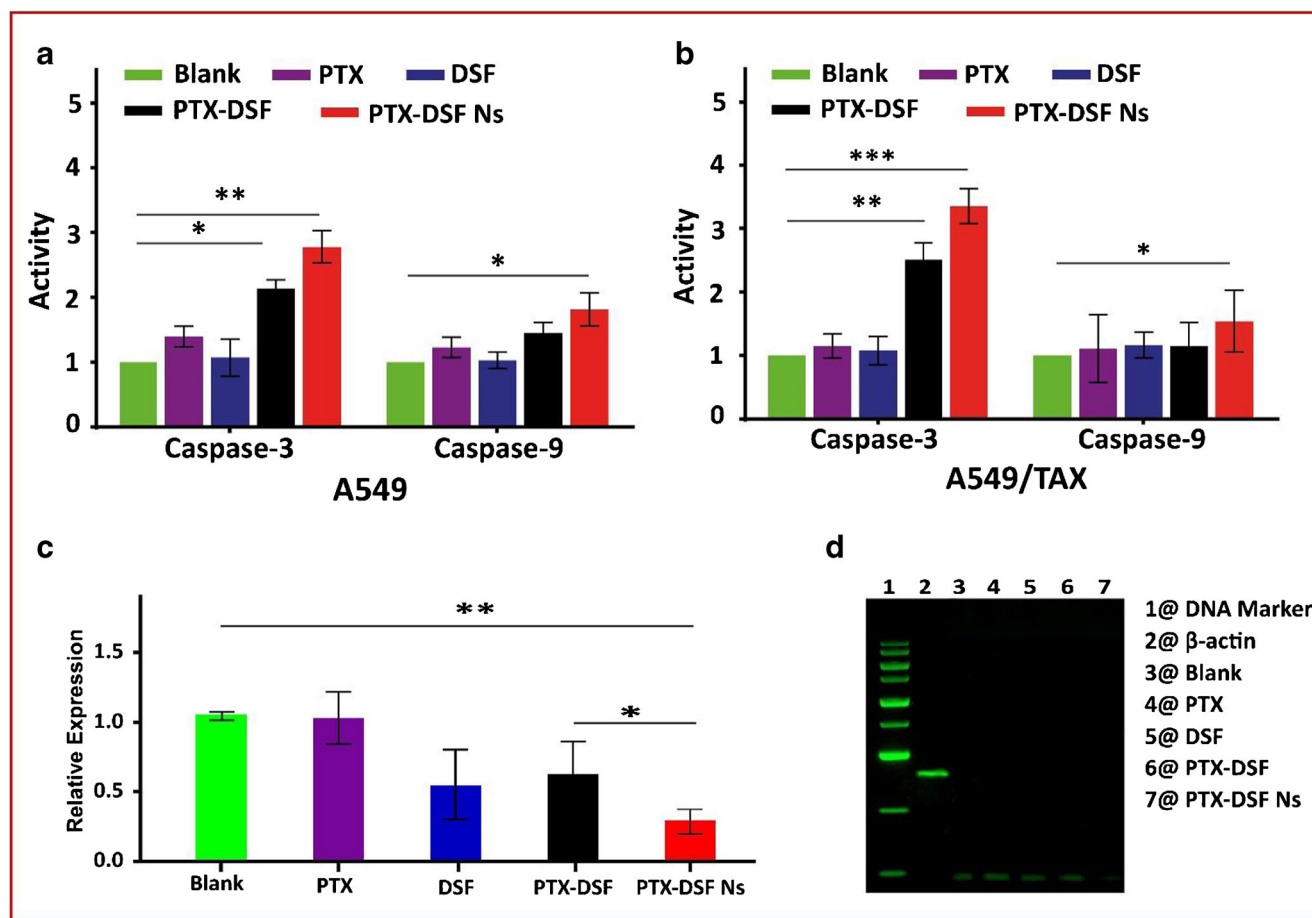


Fig. 9 Caspase-3 and -9 activity (**a, b**) of A549 and A549/TAX cells after treatment with different formulations. Determination of MDR-1 gene expressions in A549/TAX cells by (**c**) RT-qPCR and (**d**) Gel electrophoresis. The mass ratio for free-drug combination of PTX and DSF (PTX-DSF) and PTX-DSF Ns was 5:1. The cells were treated with different formulations at a PTX or DSF concentration of 5 μ g/ml for 72 h at 37°C. $n = 3$, * $P < 0.05$, ** $P < 0.01$ and *** $P < 0.001$.

discovery can be adapted to promote the uptake of nanoparticles in other types of MDR cells to improve their therapeutic outcomes. Interestingly, DSF promoted 2.5-folds and 1.8 folds increases in the number of apoptotic A549 and A549/TAX cells, respectively; these levels were as high as the cytotoxic agent PTX, indicating that DSF might represent a potential anticancer agent.

Indeed, PTX-DSF Ns are a potent strategy for enhancing the sensitivity of Taxol-resistant cells to chemotherapy. PTX is one of the most effective chemotherapeutic agents at curing various cancers (57); however, the development of drug resistance stemming from drug efflux by P-gp in cancer cells represents a major barrier to enhance the treatment efficacy (58). Hence, strategies that inactivate P-gp and inhibit drug efflux are crucial to sensitize the resistant cells to the chemotherapeutic effects of PTX. DSF reduces MDR-1 expression and significantly inhibits P-gp in A549/TAX cells, thus increasing the intracellular accumulation of PTX in PTX-DSF-treated cells and enhancing cytotoxicity. However, DSF is a very unstable drug (59,60), and the cellular uptake of the free drug is limited, markedly reducing the synergy between PTX and

DSF. Furthermore, in A549/TAX cells, the IC_{50} based on PTX in PTX-DSF Ns is decreased 1-fold compared with PTX-DSF, indicating their great potential to reduce side effects; moreover, PTX-DSF Ns induced a 1.7 folds higher apoptotic rate than PTX-DSF. The DRIs based on PTX in PTX-DSF Ns were also decreased by approximately 40% and 60% in A549 and A549/TAX cells, respectively, compared with PTX-DSF (Fig. 6). Therefore, by amplifying the synergistic mechanism, PTX-DSF Ns induce efficient cytotoxicity toward Taxol-resistant cells with a dramatic dose reduction. Overall, the present PTX-DSF Ns provide a potent strategy for combined therapy due to its extremely high drug-loading capacity, easy preparation and scale up.

CONCLUSION

In this study, a novel nanosuspension formulation for codelivery, PTX-DSF Ns, is reported, which features an extremely high drug-loading capacity for both drugs, a precise combinatory ratio, and potent cytotoxicity and apoptosis in A549 cells, particularly Taxol-resistant cells, with low IC_{50} via

a synergistic mechanism, including reduced MDR-1 expression (P-gp inactivation), upregulated caspase-3 and caspase-9 expression, and increased arrest in G2/M phase of the cell cycle. To the best of our knowledge, this report is the first to show that nanosuspensions of insoluble drugs serve as a codelivery and combined therapy system. We believe that these findings will broaden the applications of nanosuspensions in drug delivery and offers a new research avenue for nanosuspensions. In addition, this novel nanosuspension formulation is an effective approach for sensitizing Taxol-resistant cells to PTX chemotherapy and therefore has promising potential in the clinic, due to the high drug-loading capacity and easy preparation procedure. Based on our findings, PTX-DSF Ns display potent cytotoxicity toward Taxol-resistant cells along with a significant dose reduction and are a promising combined strategy for sensitizing MDR cancers to chemotherapy. In addition, the newly identified function of nanosuspensions in a combined treatment provides new research opportunities for nanosuspensions.

ACKNOWLEDGMENTS AND DISCLOSURES

This study was supported by grants from the National Natural Science Foundation of China (Nos. 81673377, 81473152, and 81402869), the Natural Science Foundation of Jiangsu Province (No. BK20140671), and the Fostering Plan of University Scientific and Technological Innovation Team and Key Members of the Outstanding Young Teacher of Jiangsu Qing Lan Project (2014 and 2016). We also thank Xiaonan Ma, Minhui Sun and Yingjian Hou from the Cellular and Molecular Biology Center of China Pharmaceutical University for providing technical assistance. The authors report no conflicts of interest with this work.

REFERENCES

- Hirsch FR, Suda K, Wiens J, Bunn PA Jr. New and emerging targeted treatments in advanced non-small-cell lung cancer. *Lancet*. 2016;388:1012–24.
- Hirsch FR, Scagliotti GV, Mulshine JL, Kwon R, Curran WJ, Wu YL, *et al.* Lung cancer: current therapies and new targeted treatments. *Lancet*. 2017;389:299–311.
- Saad M, Garbuzenko OB, Minko T. Co-delivery of siRNA and an anticancer drug for treatment of multidrug-resistant cancer. *Nanomedicine (London)*. 2008;3:761–76.
- Gao Z, Zhang L, Sun Y. Nanotechnology applied to overcome tumor drug resistance. *J Control Release*. 2012;162:45–55.
- Li W, Zhang H, Assaraf YG, Zhao K, Xu X, Xie J, *et al.* Overcoming ABC transporter-mediated multidrug resistance: molecular mechanisms and novel therapeutic drug strategies. *Drug Resist Updat*. 2016;27:14–29.
- Sandberg T, Rosenholm J, Hotokka M. The molecular structure of disulfiram and its complexation with silica. A quantum chemical study. *J Mol Struct-Theochem*. 2008;861:57–61.
- Sauna ZE, Peng XH, Nandigama K, Tekle S, Ambudkar SV. The molecular basis of the action of disulfiram as a modulator of the multidrug resistance-linked ATP binding cassette transporters MDR1 (ABCB1) and MRP1 (ABCC1). *Mol Pharmacol*. 2004;65:675–84.
- Duan X, Xiao J, Yin Q, Zhang Z, Yu H, Mao S, *et al.* Smart pH-sensitive and temporal-controlled polymeric micelles for effective combination therapy of doxorubicin and disulfiram. *ACS Nano*. 2013;7:5858–69.
- Lehar J, Krueger AS, Avery W, Heilbut AM, Johansen LM, Price ER, *et al.* Synergistic drug combinations tend to improve therapeutically relevant selectivity. *Nat Biotechnol*. 2009;27:659–66.
- Hu CMJ, Aryal S, Zhang L. Nanoparticle-assisted combination therapies for effective cancer treatment. *Ther Deliv*. 2010;1:323–34.
- Mehra NK, Jain K, Jain NK. Pharmaceutical and biomedical applications of surface engineered carbon nanotubes. *Drug Discov Today*. 2015;20:750–9.
- Misra R, Acharya S, Sahoo SK. Cancer nanotechnology: application of nanotechnology in cancer therapy. *Drug Discov Today*. 2010;15:842–50.
- Gao H. Progress and perspectives on targeting nanoparticles for brain drug delivery. *Acta Pharm Sin B*. 2016;6:268–86.
- Shen Y, Jin E, Zhang B, Murphy CJ, Sui M, Zhao J, *et al.* Prodrugs forming high drug loading multifunctional nanocapsules for intracellular cancer drug delivery. *J Am Chem Soc*. 2010;132:4259–65.
- Guo S, Lin CM, Xu Z, Miao L, Wang Y, Huang L. Co-delivery of cisplatin and rapamycin for enhanced anticancer therapy through synergistic effects and microenvironment modulation. *ACS Nano*. 2014;8:4996–5009.
- Rabinow BE. Nanosuspensions in drug delivery. *Nat Rev Drug Discov*. 2004;3:785–96.
- He W, Xin X, Li Y, Han X, Qin C, Yin L. Rod-shaped drug particles for cancer therapy: the importance of particle size and participation of caveolae pathway. *Part Part Syst Charact*. 2017;34(6)
- He W, Wang Y, Lv Y, Xiao Q, Ye L, Cai B, *et al.* Denatured protein stabilized drug nanoparticles: tunable drug state and penetration across the intestinal barrier. *J Mater Chem B*. 2017;5:1081–97.
- Attili-Qadri S, Karra N, Nemirovski A, Schwob O, Talmon Y, Nassar T, *et al.* Oral delivery system prolongs blood circulation of docetaxel nanocapsules via lymphatic absorption. *P Natl Acad Sci USA*. 2013;110:17498–503.
- Fuhrmann K, Gauthier MA, Leroux JC. Targeting of injectable drug nanocrystals. *Mol Pharm*. 2014;11:1762–71.
- Müller RH, Gohla S, Keck CM. State of the art of nanocrystals – special features, production, nanotoxicology aspects and intracellular delivery. *Eur J Pharm Biopharm*. 2011;78:1–9.
- Lu Y, Qi J, Dong X, Zhao W, Wu W. The in vivo fate of nanocrystals. *Drug Discov Today*. 2017;22:744–50.
- Gao H. Perspectives on dual targeting delivery systems for brain tumors. *J Neuroimmune Pharmacol*. 2017;12:6–16.
- Li Y, Wu Z, He W, Qin C, Yao J, Zhou J, *et al.* Globular protein-coated paclitaxel nanosuspensions: interaction mechanism, direct cytosolic delivery, and significant improvement in pharmacokinetics. *Mol Pharm*. 2015;12:1485–500.
- He W, Lu Y, Qi J, Chen L, Hu F, Wu W. Food proteins as novel nanosuspension stabilizers for poorly water-soluble drugs. *Int J Pharm*. 2013;441:269–78.
- Zhao R, Hollis CP, Zhang H, Sun L, Gemeinhart RA, Li T. Hybrid nanocrystals: achieving concurrent therapeutic and bioimaging functionalities toward solid tumors. *Mol Pharm*. 2011;8:1985–91.
- Chen SY, Hu SS, Dong Q, Cai JX, Zhang WP, Sun JY, *et al.* Dong. Establishment of paclitaxel-resistant breast cancer cell line and

- nude mice models, and underlying multidrug resistance mechanisms in vitro and in vivo. *Asian Pac J Cancer Prev.* 2013;14: 6135–40.
28. Jiang N, Dong XP, Zhang SL, You QY, Jiang XT, Zhao XG. Triptolide reverses the taxol resistance of lung adenocarcinoma by inhibiting the NF- κ B signaling pathway and the expression of NF- κ B-regulated drug-resistant genes. *Mol Med Rep.* 2016;13: 153–9.
 29. Chou T-C. Theoretical basis, experimental design, and computerized simulation of synergism and antagonism in drug combination studies. *Pharmacol Rev.* 2006;58:621–81.
 30. Tallarida RJ. An overview of drug combination analysis with isobolograms. *J Pharmacol Exp Ther.* 2006;319:1–7.
 31. Li J, Yang YL, Li LZ, Zhang L, Liu Q, Liu K, *et al.* Succinate accumulation impairs cardiac pyruvate dehydrogenase activity through GRP91-dependent and independent signaling pathways: therapeutic effects of ginsenoside Rb1. *Biochim Biophys Acta.* 2017;1863(11):2835–47.
 32. Ha HK, Kim JW, Lee MR, Jun W, Lee WJ. Cellular uptake and cytotoxicity of β -lactoglobulin nanoparticles: the effects of particle size and surface charge. *Asian Australas J Anim Sci.* 2015;28:420–7.
 33. Song W, Tang Z, Lei T, Wen X, Wang G, Zhang D, *et al.* Stable loading and delivery of disulfiram with mPEG-PLGA/PCL mixed nanoparticles for tumor therapy. *Nanomed-Nanotechnol.* 2016;12: 377–86.
 34. Duan X, Li Y. Physicochemical characteristics of nanoparticles affect circulation, biodistribution, cellular internalization, and trafficking. *Small.* 2013;9:1521–32.
 35. Shen XC, Liou XY, Ye LP, Liang H, Wang ZY. Spectroscopic studies on the interaction between human hemoglobin and CdS quantum dots. *J Colloid Interf Sci.* 2007;311:400–6.
 36. Gorinstein S, Goshev I, Moncheva S, Zemser M, Weisz M, Caspi A, *et al.* Intrinsic tryptophan fluorescence of human serum proteins and related conformational changes. *J Protein Chem.* 2000;19: 637–42.
 37. Clayton AH, Sawyer WH. Site-specific tryptophan fluorescence spectroscopy as a probe of membrane peptide structure and dynamics. *Eur Biophys J Biophys.* 2002;31:9–13.
 38. Chadborn N, Bryant J, Bain AJ, Shea PO. Ligand-dependent conformational equilibria of serum albumin revealed by tryptophan fluorescence quenching. *Biophys J.* 1999;76:2198–207.
 39. Roach P, Farrar D, Perry CC. Interpretation of protein adsorption: surface-induced conformational changes. *J Am Chem Soc.* 2005;127:8168–73.
 40. Brewer SH, Glomm WR, Johnson MC, Knag MK, Franzen S. Probing BSA binding to citrate-coated gold nanoparticles and surfaces. *Langmuir.* 2005;21:9303–7.
 41. Gao D, Tian Y, Bi S, Chen Y, Yu A, Zhang H. Studies on the interaction of colloidal gold and serum albumins by spectral methods. *Spectrochim Acta A.* 2005;62:1203–8.
 42. Xiao Q, Huang S, Qi ZD, Zhou B, He ZK, Liu Y. Conformation, thermodynamics and stoichiometry of HSA adsorbed to colloidal CdSe/ZnS quantum dots. *Biochimica et Biophysica Acta (BBA) - Proteins and Proteomics.* 2008;1784:1020–7.
 43. Jiang L, Yang BQ, Ma YD, Liu YC, Yang WS, Li TJ, *et al.* The binding of phosphorothioate oligonucleotides to CdS nanoparticles. *Chem Phys Lett.* 2003;380:29–33.
 44. Kelly SM, Jess TJ, Price NC. How to study proteins by circular dichroism. *Biochimica et Biophysica Acta (BBA) - Proteins and Proteomics.* 2005;1751:119–39.
 45. Zhang L, Xiao Q, Wang Y, Zhang C, He W, Yin L. Denatured protein-coated docetaxel nanoparticles: alterable drug state and cytosolic delivery. *Int J Pharm.* 2017;523:1–14.
 46. Loo TW, Clarke DM. Blockage of drug resistance in vitro by disulfiram, a drug used to treat alcoholism. *J Natl Cancer Inst.* 2000;92: 898–902.
 47. Fasseeh H, Dinarvand R, Ghavamzadeh A, Esfandiyari-Manesh M, Moradian H, Faghili S, *et al.* Delivery of disulfiram into breast cancer cells using folate-receptor-targeted PLGA-PEG nanoparticles: in vitro and in vivo investigations. *J Nanobiotechnol.* 2016;14: 32.
 48. Cintron-Colonand R, Vega I. Molecular mechanism of paclitaxel-induced degradation of SCG10: a potential neuropathy biomarker. *FASEB J.* 2014;28:651–14.
 49. Saw PE, Park J, Jon S, Farokhzad OC. A drug-delivery strategy for overcoming drug resistance in breast cancer through targeting of oncofetal fibronectin. *Nanomed-Nanotechnol.* 2017;13:713–22.
 50. Gao L, Liu G, Ma J, Wang X, Zhou L, Li X. Drug nanocrystals: in vivo performances. *J Control Release.* 2012;160:418–30.
 51. Chen Y, Li T. Cellular uptake mechanism of paclitaxel nanocrystals determined by confocal imaging and kinetic measurement. *AAPS J.* 2015;17:1126–34.
 52. Fuhrmann K, Polomska A, Aeberli C, Castagner B, Gauthier MA, Leroux JC. Modular design of redox-responsive stabilizers for nanocrystals. *ACS Nano.* 2013;7:8243–50.
 53. Hu Q, Sun W, Wang C, Gu Z. Recent advances of cocktail chemotherapy by combination drug delivery systems. *Adv Drug Deliv Rev.* 2016;98:19–34.
 54. Noh J, Kwon B, Han E, Park M, Yang W, Cho W, *et al.* Amplification of oxidative stress by a dual stimuli-responsive hybrid drug enhances cancer cell death. *Nat Commun.* 2015;6:6907.
 55. Chen YZ, Zhang M, Jin HY, Tang YS, Wu AH, Huang YZ. Prodrug-like, PEGylated protein toxin trichosanthin for reversal of chemoresistance. *Mol Pharm.* 2017;14:1429–38.
 56. Ni J, Tian FC, Dahmani FZ, Yang H, Yue DR, He SW, *et al.* Curcumin-carboxymethyl chitosan (CNC) conjugate and CNC/LHR mixed polymeric micelles as new approaches to improve the oral absorption of P-gp substrate drugs. *Drug Deliv.* 2016;23:3424–35.
 57. Baird RD, Tan DS, Kaye SB. Weekly paclitaxel in the treatment of recurrent ovarian cancer. *Nat Rev Clin Oncol.* 2010;7:575–82.
 58. Liu Y, Huang L, Liu F. Paclitaxel nanocrystals for overcoming multidrug resistance in cancer. *Mol Pharm.* 2010;7:863–9.
 59. Johansson B. Stabilization and quantitative determination of disulfiram in human plasma samples. *Clin Chim Acta.* 1988;177:55–63.
 60. B. Johansson. A review of the pharmacokinetics and pharmacodynamics of disulfiram and its metabolites. *Acta psychiatrica Scandinavica Supplementum.* 1992;369:15–26.